From Vacuum Tubes to Modern Semiconductors

Opportunities for Industrial Heating Industry

Ahmad, Faheem; Aunsborg, Thore Stig; Jørgensen, Asger Bjørn; Munk-Nielsen, Stig

Published in:
I E E E Transactions on Industry Applications

DOI (link to publication from Publisher):
10.1109/TIA.2024.3397639

Publication date:
2024

Document Version
Accepted author manuscript, peer reviewed version

This is a post-print of the accepted manuscript submitted to IEEE Transactions on Industry Applications.

From Vacuum Tubes to Modern Semiconductors: Opportunities for Industrial Heating Industry

Faheem Ahmad, Thore Stig Aunsborg, Asger Bjørn Jørgensen, and Stig Munk-Nielsen, *Member, IEEE*

***Abstract*—Industrial heating plays a significant role in the modern society. It constitutes about 20% of the global energy consumption. Modern industrial heating plants (especially induction and dielectric heating) uses vacuum tube triode based radio frequency (RF) generator. The vacuum tube RF generator provides an efficiency of 60% or less. This is not optimum, as almost half of the energy is being wasted as heat. Modern semiconductor technology based on wide bandgap (WBG) materials such as silicon carbide (SiC) and gallium nitride (GaN) provides an opportunity to remove the ageing vacuum tube from industrial heating plants. However the industrial heating plants requires high voltage output from the RF generator to deliver high power which has been a technological barrier towards semiconductor implementation in industrial heating industry. In this paper a method is proposed to series connect multiple RF converters to scale-up the output voltage from semiconductor based RF generator. Class-PN is used as RF converter to demonstrate the proposed multi-cell series connection method. Furthermore a controller scheme is presented that allows individual Class-PN RF converter to maintain optimum operation without the need of communication between each cells. For the small-scale prototype three Class-PN cells are operated in multi-cell configuration to boost the DC input of 185 V to peak-peak RF voltage of 1.1 kV at 6.78 MHz. Output power of 856 W at an efficiency of 80% from DC input to RF load is demonstrated.**

***Index Terms*—Gallium nitride (GaN) devices, industrial heating, multi-cell converters, radio frequency (RF) converters.**

I. Introduction

INDUSTRIAL heating plays a significant role in moulding modern human lifestyle. It is evident from the fact that industrial heating constitutes 20% of the world total energy consumption and more than 50% of direct greenhouse gas emission of USA [1]. Industrial heating is used in multiple applications for example in baking and packaging of food products, paper and pulp industry, melting and annealing of metals. There are broadly three basic categories of industrial heating based on how the heat is generated: fuel-based heating, steam-based heating, and electric-based heating [2]. However in this article the focus is solely on electric-based industrial heating where electrical energy is converted directly into heat in the work material. This excludes conduction heating where a resistive element generates heat which is transferred to the work material. Electric-based industrial heating can be classified into different categories based on the frequency of operation and the work material as shown in Fig. 1 [1].

This work is supported by the Greenheat project which is sponsored by Innovation Fund Denmark, and is a collaboration between Topsil Globalwafers A/S, Kallesoe Machinery A/S, and Aalborg University. The Greenheat project is stated to run for three years from 2023-2026 and aims to develop and demonstrate two full-scale prototypes of radio frequency generators that replaces existing vacuum tube triode based RF generators in the industry.

Frequency	50 Hz – 500 kHz	2 – 100 MHz	200 – 3000 MHz	30 – 400 THz
	Induction 	Radio 	Microwave 	Infrared 
Max temp °C	3000	2000	2000	2200
ISM band				
Efficiency	50 – 90%	80%	80%	60 – 90%
Application	Rapid internal heating of metals.	Rapid internal heating of large volumes.	Rapid internal heating of large volumes.	Very rapid heating of surfaces and thin materials.

Fig. 1. Different electrification heating methodologies and frequencies at which they are operated [1].

Induction heating has been used since early 20th century for internal heating in metal work materials. When passing an alternating magnetic field through conductive materials it generates eddy currents in the material that induces heat. The frequency of operation for induction heating ranges from 50 kHz in high volume metal production to few MHz for silicon crystal growth [3], [4]. In applications where non-conductive work material is to be heated, both radio (also referred as dielectric) and microwave heating can be applied such as in drying cross-laminated wood, paper and pulp industry, drying ceramic products, food baking and packaging etc. The frequency range usually identified for the different electric-heating methodologies are indicated in Fig. 1. For high throughput in heating non-conductive materials, usually dielectric heating is preferred over microwave as the longer wavelength radio waves in dielectric heating penetrates deeper in the work material. Within the range of 2-100 MHz, the frequency bands allocated by governments authorities for industrial heating purposes are 6.78, 13.56, 27.12, or 40.68 MHz. The frequency bands are referred as ISM band as they are reserved for industrial, scientific and medical applications. However induction heating applications operating below 2-3 MHz have no such guidelines or restrictions. The efficiency values indicated in Fig. 1 represent the efficiency with which electric energy can be converted into heat in the work material.

The high frequency operation at multi-MHz in the induction and dielectric heating industries have been historically achieved by vacuum tube triodes as RF generator [5]. Fig. 2 shows a simplified schematic of a vacuum tube triode in an induction or dielectric heating plant. The triode generates the radio frequency (RF) output which is transformed through transformer to match the load. The capacitive tuning element on the secondary side is used to either match the varying

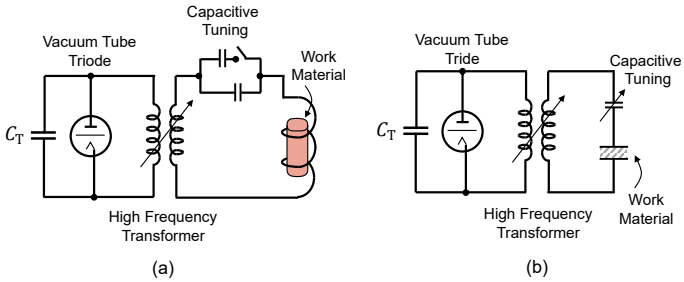

Fig. 2. Schematic of vacuum tube triode coupled via high frequency transformer to work material (a) in induction heating, and (b) dielectric heating [5].

impedance of the work material or / and control the power being delivered. Taking the case of dielectric heating, the power density being delivered to the work material can be defined as (1) [6],

$$P = k \cdot f \cdot \epsilon \cdot \tan\delta \cdot E^2 \tag{1}$$

Where k is proportionality constant, f is triode frequency, ϵ is dielectric permittivity of the work material, $\tan\delta$ is loss tangent, and E is electric field strength of the RF voltage applied to the work material defined as $E = V/d$, where V is the voltage applied on the work material and d is the thickness of the work material. Therefore in principle it should be possible to increase the power dissipated in the dielectric by merely increasing either frequency (f) or the applied voltage (V), given the remaining parameters in (1) are based on work material properties. However, in practical considerations there are limiting factors. For example, as the triode frequency is increased it can lead to standing waves on the electrodes causing non-uniform heating, or value of inductance required for tuning is decreased to an unachievable minimum causing difficulty in tuning, and most importantly the losses in triode increases rapidly with increasing operation frequency. The other controlled variable, voltage applied (V) can also be increased to increase the heat dissipation. However, at very high voltages corona discharge starts to take place which leads to voltage breakdown. A reliable and reproducible upper limit of voltage has usually been found to be approximately 10 kV [7].

The high voltage and radio frequency requirement has led the induction and dielectric heating industries to be completely reliant on vacuum tube RF generator. Although the vacuum tube RF generator are highly inefficient, offering efficiencies of only 60% [6], [8]. This does not need to be the case anymore as modern semiconductor technology have achieved MHz operation in RF region with an efficiency of more than 90%. Thus it presents as an opportunity for the industrial heating industry to incorporate semiconductor based RF generator and phase out the ageing vacuum tube technology. In section II the state-of-art semiconductor based high frequency converters are summarized. The achievements of high frequency operation of modern semiconductor technology has been presented along with the challenges that restricts its implementation in industrial heating industry. Section III presents the four-switch resonant converter topology Class-PN that will be used as high frequency converter. The controller design for a single Class-PN is presented in section IV. The controller is designed to ensure independent operation of individual Class-PN converter. Finally in section V, the proposed series connection method to achieve multi-cell operation is presented which is experimentally validated in section VI. Section VII summarizes the results.

II. State-of-Art High Frequency Converters

Historically in power electronics, silicon (Si) devices have not been considered for operation at multi-MHz switching frequency. However there have been few works such as [9], [10], which are based on Si RF MOSFETs from IXYS have demonstrated 5 kW at 89% and 1 kW at 85% efficiency at 13.56 MHz respectively. Though the Si RF MOSFET from IXYS have been discontinued. Other work using Si device in a high frequency converter was presented at a lower power of only 23 W at 6.78 MHz [11]. The advent of modern semiconductor technology such as wide bandgap (WBG) devices have demonstrated superior performance at MHz switching operation compared to Si devices. Fig. 3 cites output power and operation frequency achieved by some state-of-art converters based on WBG materials utilizing silicon carbide (SiC) or gallium nitride (GaN) devices [12]–[20]. The work in [17] is based on GaN device operating at 6.78 MHz and achieves an efficiency of 95.7% at 1.7 kW. From Fig. 3 it can be understood that SiC devices are preferred for switching frequency under 4 MHz (except [14]). This is suitable for industrial induction heating applications as the maximum frequency required in induction heating is usually few MHz as seen in silicon crystal growth [4]. For example the work in [19] is based on 1700 V SiC MOSFET (CPM2-1700-0080B) operating at 2.5 MHz for induction heating application and achieves 91% efficiency at 5 kW. For dielectric heating that requires ISM band frequency of 6.78 or 13.56 MHz, GaN devices are better suited for switching frequency beyond 4 MHz and have been demonstrated in other applications as well like wireless power transfer [16], [17], [20]. All the three works are based on 650 V GaN HEMT device. A research group from Stanford University have showcased 13.56 MHz operation using both SiC (900V C3M0065090J) and GaN (650V GS66508B) devices with an output efficiency of 94% [12], [14].

Based on the literature survey a qualitative comparison matrix of different technology for RF generator towards industrial heating applications can be developed. In Table I a comparison between the vacuum tube, silicon as well as next generation WBG (SiC and GaN) material based MOSFET is presented. Vacuum tube has been successful so far because of its superior voltage, frequency and output power capability. However the losses incurred in a vacuum tube RF generator is significant. Furthermore, across the world there are fewer manufacturers of vacuum tube and thus it is not sustainable for the industry. Silicon based power semiconductor technology have matured over the decades and can attain the high voltage requirement to a certain extent, however they are not suitable for RF operation

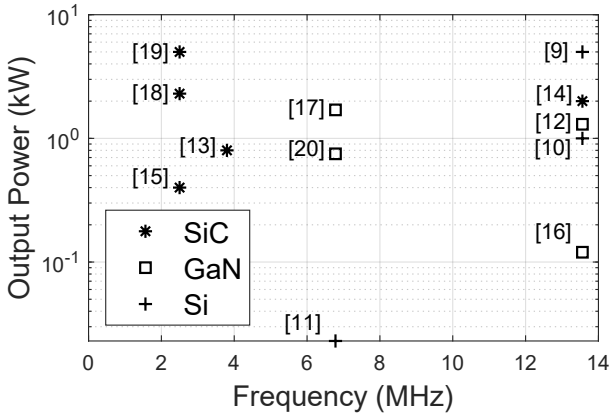

Fig. 3. Frequency of operation and output power achieved by state-of-art solid-state converter.

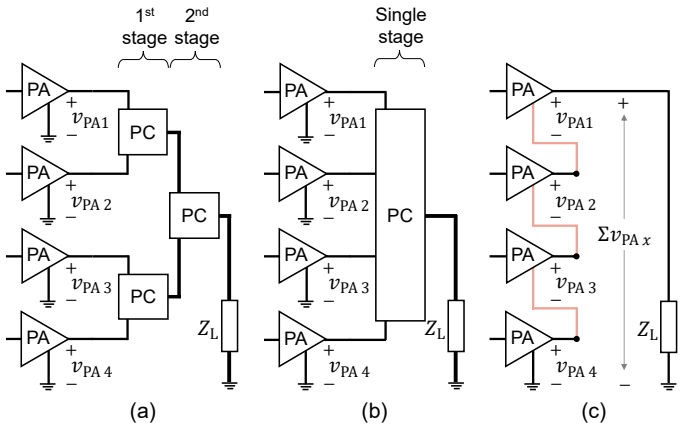

Fig. 4. Different strategies to connect multiple power amplifers (PA) (a) staggered power combiner (PC) [21], [22], (b) single-stage PC [23], and (c) series connection of PA proposed in this paper.

as seen by low efficiencies in [9], [10]. WBG materials have demonstrated the high frequency operation and SiC based MOSFETs are available in high voltage rating compared to GaN devices. However the switching losses incurred in SiC device is higher compared to the GaN and thus restricts its operation under 4 MHz as seen in the literature survey. Nevertheless the biggest challenge with semiconductor based RF generator for industrial heating application is the output power limitation. As seen in Fig. 3 the semiconductor based multi-MHz converter are mainly limited to under 10 kW.

TABLE I
COMPARISON OF VACUUM TUBE, SILICON (SI), AND WBG TRANSISTOR TECHNOLOGY

Characteristics	Vacuum Tube	Vertical Si	SiC	GaN
Voltage	+++	+	++	−
Frequency	+++	−	+	++
Power Loss	−−	−	+	++
RF Output Power	++	+	+	−
Future Proof	−−	+	++	++

In very-high frequency (VHF) and ultra-high frequency (UHF) applications, in order to increase the output power a standard strategy has been to use power combiners [21]. The structure is shown in Fig. 4(a) where PA stands for power amplifier which is a high frequency converter. As shown in the figure that the output power of two PAs are combined using a power combiner (PC). Then the output from the 1st stage PCs are combined in the 2nd stage. This is a staggered approach of combining output power from multiple high frequency converters [21], [22]. Another approach to combine power from multiple PAs is to use a single stage power combiner as shown in Fig. 4(b) [23]. The power combiner strategy solves the output power limitation of a single semiconductor based high frequency converter however it adds additional component in the circuit. Furthermore the RF generator in industrial heating industry is required to generate high voltage output. Therefore a semiconductor based RF converter using power combiner will not be able to retrofit into an existing plant.

In this paper we propose a method to combine the power from several PAs without using power combiner. The proposed method links up the output terminals of each PAs in a series connection to scale-up the output voltage. The proposed method is illustrated in Fig. 4(c) [24]. Next section presents a high frequency, voltage source type, resonant converter topology Class-PN that is used as individual power amplifiers which are then series connected to scale-up the output voltage.

III. FOUR-SWITCH RESONANT CONVERTER TOPOLOGY CLASS-PN

RF converters are normally based on soft-switching operation of the semiconductor devices. The state-of-art converters presented in Fig. 3 are all based on soft-switched resonant converter topologies such as Class-E, Class-EF$_2$, Class-Φ_2 etc. Under ideal conditions, a soft-switched semiconductor device generate zero switching loss which is crucial when operating at multi-MHz. This is achieved by resonant charging-discharging of the output capacitance (C_{OSS}) of the semiconductor device by an external reactive element in every cycle. Thus under ideal operations increasing the current rating of GaN devices will only increase the reactive power required to achieve soft-switching operation. However, there are growing number of literature demonstrating that soft-switching of GaN or SiC devices are not completely loss-less. A dissipation energy (E_{diss}) is lost every time resonant charging-discharging of C_{OSS} is conducted which becomes a dominant loss factor when operating at multi-MHz [25], [26]. Thus employing high current rated GaN device to increase RF generator output power will have high C_{OSS} value and thus high E_{diss} resulting in larger switching losses. Therefore another challenge for the power electronics engineer designing GaN based RF generators is maximizing the RF power delivered from a specific GaN device. Class-PN is a voltage source converter that also achieves high frequency operation using zero voltage switching (ZVS) resonant operation between load reactance and C_{OSS}. When the load current is inductive, it charges and

discharges the C_{OSS} and the GaN device achieves zero voltage across its drain-source during the dead time and thus soft-switches when the gate is turned-on. The phenomenon of ZVS for voltage source type topology is explained in [27]. The switching mechanism and voltage/current waveforms of the four GaN devices in Class-PN are illustrated in detail in [28]. The four switches of Class-PN cell are GaN devices (GS66506T) from Gansystems rated at 650 V and 22.5 A. The device provides a superior output junction capacitance (C_{OSS}) of only 49 pF at 400 V [29]. These GaN devices are based on GaNPX package design that have a top side thermal pad that allows for attaching the heatsink away from the electrical drain, source and gate pads which are present on the bottom side soldered directly to PCB. The concept is shown in Fig. 5 [30]. For the current paper a 0.5 mm Gap-pad with a thermal conductivity of 5 W/mK is used as thermal interface material between the top side thermal pad and heatsink [31]. This leads to a junction-ambient thermal resistance ($R_{th(\text{JA})}$) of 4.9°C/W. The presented cooling solution and other approaches considered for Class-PN have been covered in [32]. For future work the authors are considering a direct bonded copper (DBC) based design where a hybrid DBC/PCB design will be used for a better thermal performance. The hybrid design will be similar to what has been published in [33].

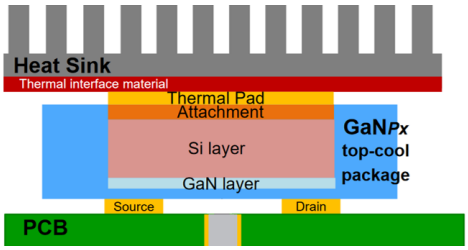

Fig. 5. Structure of GaNPX package for Gansystems top side cooled devices [30].

However unlike single-switch topologies like Class-E, the Class-PN delivers more than 6x higher output power using the same GaN device type. This is explained by the power handling capability of the resonant topology [28]. Power handling capability (c_p) is defined by the ratio of maximum voltage subjected to semiconductor switch drain-source (V_{SM}) to the DC link voltage (V_{DC}), multiplied by the ratio of peak current through the switch (I_{SM}) and the DC current (I_{DC}). Table II shows the c_p of a few resonant topologies. Some of the advantages and disadvantages of the topologies in Table II are explained here. Class-E is a popular resonant topology due to its low component count and ease of operation. However it has a low power handling capability compared to all the other resonant switching topologies presented in Table II. This is due to the high voltage and current stress subjected to the semiconductor switch in Class-E. Over the years there have been several single-switch resonant topology derivatives. Both Class-EF_2 and Class-Φ_2 combined the efficient switching capability of Class-E with the improved switch voltage and current waveforms of Class-F and Class-F^{-1}. This leads to improved power handling capability for both Class-EF_2 and Class-Φ_2 compared to Class-E while still retaining the simplicity of single switch topology. The disadvantage however is that both Class-EF_2 and Class-Φ_2 contain multiple resonant components which must be tuned for proper operation. These resonant components can sometimes interact with each other making it difficult to work with them [34]. Class-D is a popular resonant topology for amplifier applications, which provides significantly higher power handling capability compared to the single switch topologies. However the requirement of dead time and high side gate drive makes its implementation a challenge at very high switching frequency. The challenges observed for Class-D are the same for Class-PN and full-bridge (FB) as well. However by further increasing the number of semiconductor devices from two to four, both Class-PN and FB increase the power handling capability by another factor of 2. Utilizing the definition of power handling capability one can calculate the maximum theoretical power ($P_{\text{max(TH)}} = c_p \cdot V_{\text{SM}} I_{\text{SM}}$) that can be achieved by such resonant topologies. For example, when the semiconductor device is subjected to a V_{SM} of 450 V and I_{SM} of 15 A. Class-PN has $P_{\text{max(TH)}}$ calculated to be 4.3 kW which is more than 6x of Class-E. However, even though Class-PN increases device utilization, a single cell with an output power of 4.3 kW will be insufficient for industrial heating applications as discussed in section II. And therefore the Class-PN will be expanded to multi-cell operation using the proposed method in Fig. 4(c).

TABLE II
THEORETICAL OUTPUT POWER LIMIT WHEN SEMICONDUCTOR DEVICE SUBJECTED TO MAX. 450 V, 15 A

Topology	Switches	c_p	$P_{\text{max(TH)}}$ (kW)
Class-E [10], [15], [18]	1	0.09	0.66
Class-EF_2 [11]	1	0.13	0.89
Class-Φ_2 [12], [14], [17]	1	0.16	1.08
Class-D [9], [13]	2	0.32	2.15
Class-PN, FB [28]	4	0.64	4.30

IV. ANALYSIS OF A SINGLE CLASS-PN CELL

Operating converters at several MHz leads to a very short time period, for example at 6.78 MHz the time period is only 147.5 ns. Thus implementing central controller scheme that communicates with individual converters will not be feasible. Therefore in the proposed approach of series connecting the power amplifiers as shown in Fig. 4(c), the idea is to implement a local controller within each Class-PN converter that is able to ensure its own optimum operation. To achieve it in this section the capacitor voltage balancing of a single Class-PN cell is explained and the controller designed to ensure it.

A. Capacitor Voltage Balancing Mechanism in Class-PN

Class-PN consists of four-switches, a capacitor (C) and two coupled inductors (L_1, L_2) as shown in Fig. 6(a). For stable operation of Class-PN in multi-cell configuration, it is necessary to ensure balanced voltage of the capacitor, C.

Therefore, the voltage balancing mechanism of capacitor (C) is presented. The load current path during the P-state and N-state is indicated in Fig. 6(a). In [28] the switching scheme for the four-switches of Class-PN is presented. When $Q1$ and $Q4$ turns-on, a positive voltage rise is seen in load Z_{RF} during the P-state and vice-versa for the N-state. In Fig. 6(b) the switches have been replaced with an equivalent voltage drop v_{SW} for P-state in black and N-state in grey. And the voltage across coupled inductors L_1, and L_2 are shown as v_1, and v_2 respectively. Fig. 6(c) shows the inductor voltages $v_1(t)$, and $v_2(t)$ during the initial transient stage when the capacitor voltage (v_{C}) is charging up to DC link voltage (V_{DC}). T represents the switching period.

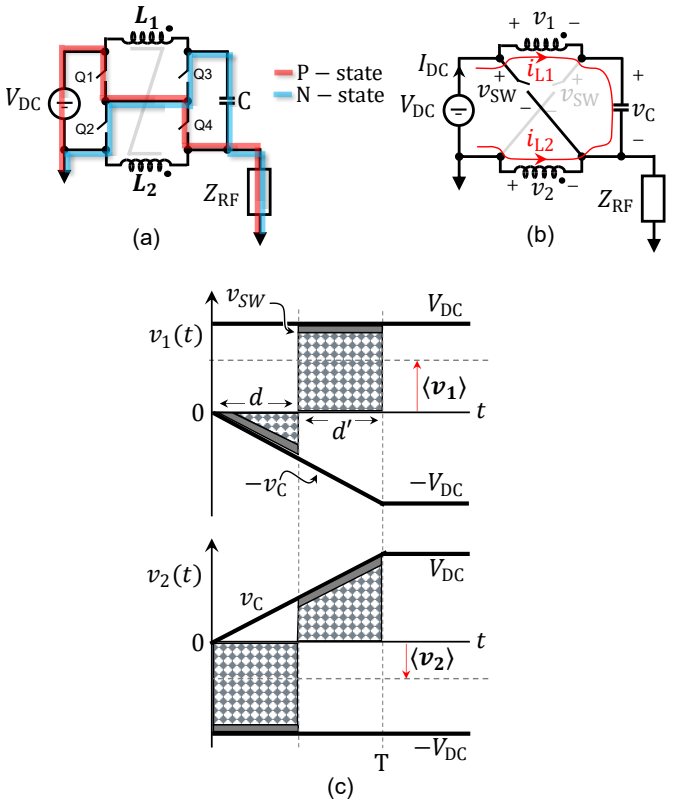

Fig. 6. (a) Current paths during the P-state, and N-state highlighted, (b) equivalent voltage loops of Class-PN, (c) average voltage across the inductor L_1 and L_2 during the transient stage at d = 0.5.

$$v_1(t) = \begin{cases} v_{\mathrm{SW}} - v_{\mathrm{C}} & \in \quad t = d\mathrm{T} \\ V_{\mathrm{DC}} - v_{\mathrm{SW}} & \in \quad t = d'\mathrm{T} \end{cases}$$
$$v_2(t) = \begin{cases} v_{\mathrm{SW}} - V_{\mathrm{DC}} & \in \quad t = d\mathrm{T} \\ v_{\mathrm{C}} - v_{\mathrm{SW}} & \in \quad t = d'\mathrm{T} \end{cases} \tag{2}$$

$$\langle v_1(t)\rangle + \langle v_2(t)\rangle = (v_{\mathrm{SW}} - v_{\mathrm{C}}) \cdot d\mathrm{T} + (V_{\mathrm{DC}} - v_{\mathrm{SW}}) \cdot d'\mathrm{T} + (v_{\mathrm{SW}} - V_{\mathrm{DC}}) \cdot d\mathrm{T} + (v_{\mathrm{C}} - v_{\mathrm{SW}}) \cdot d'\mathrm{T} \tag{3}$$

$$\langle v_1(t)\rangle + \langle v_2(t)\rangle = (v_{\mathrm{C}} + V_{\mathrm{DC}} - 2 \cdot v_{\mathrm{SW}}) \cdot (d' - d)\mathrm{T} \tag{4}$$

Fig. 6(b) is used to write the inductor voltage $v_1(t)$, and $v_2(t)$ as shown in (2). In (3) the total average inductor voltage

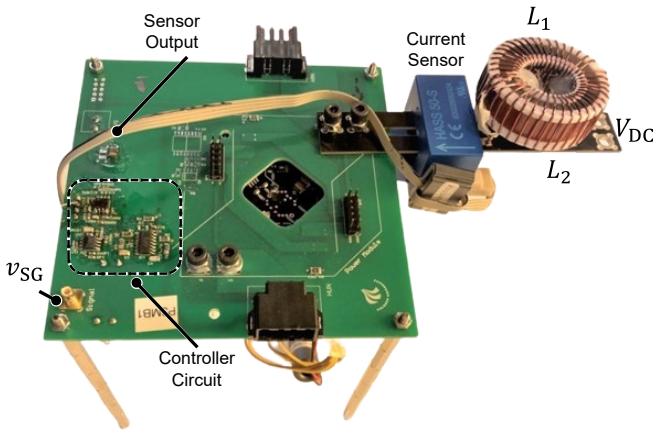

Fig. 7. Coupled inductors L_1, L_2 connected to Class-PN, and current sensor based compensation circuit.

$\langle v_1(t)\rangle + \langle v_2(t)\rangle$ is shown and finally simplified in (4). Under steady-state condition the capacitor voltage v_{C} is equal to V_{DC} and the average inductor voltages $\langle v_1(t)\rangle$, and $\langle v_2(t)\rangle$ are 0. Thus at steady-state, d = 0.5 ensures the equality of (4). However during the transient stage, for example when the capacitor (C) is getting charged v_{C} has not reached V_{DC} and thus $|\langle v_1(t)\rangle| \neq |\langle v_2(t)\rangle|$ as shown in Fig. 6(c). Therefore the duty cycle (d) has to be varied to ensure the equality of (4). This is achieved by maintaining equal amplitude of average current in the coupled inductors, i.e., $|i_{\mathrm{L1}}| = |i_{\mathrm{L2}}|$. The coupled inductors are designed in order of μH, thus it allows DC current to charge the cell capacitor, while RF current at 6.78 MHz will be rejected or has significantly small value due to the high impedance at this frequency. A controller is implemented in Class-PN to achieve this functionality and is presented next.

B. Controller Design

As discussed the controller in Class-PN topology is based on maintaining equal value of average current in the coupled inductors, i.e., $|i_{\mathrm{L1}}| = |i_{\mathrm{L2}}|$. In Fig. 6(b) the inductor currents are shown as flowing in the same direction, thus under optimum condition $I_{\mathrm{L1}} = -I_{\mathrm{L2}}$ which are DC component of inductor current. Thus the condition to maintain for the controller circuit is given in (5),

$$I_{\mathrm{L1}} + I_{\mathrm{L2}} = 0 \tag{5}$$

The coupled inductors are developed on a ultra-high frequency powder based toroidal core from Micrometals with a nominal A_L value of 12 $\mathrm{nH/N^2}$ and an initial relative permeability of 10 [35]. Fig. 7 shows the coupled inductors L_1 and L_2 on the high frequency toroidal core. The coupled inductor is connected to the Class-PN via a black PCB as a busbar. A 50 A rated current sensor (LEM HASS 50-S) is used to measure the total current as given in (5). Fig. 7 also shows the controller circuit that receives input from the current sensor.

Fig. 8 is the schematic of current-mode controller design as well as the PWM generation for the four-switches in a single

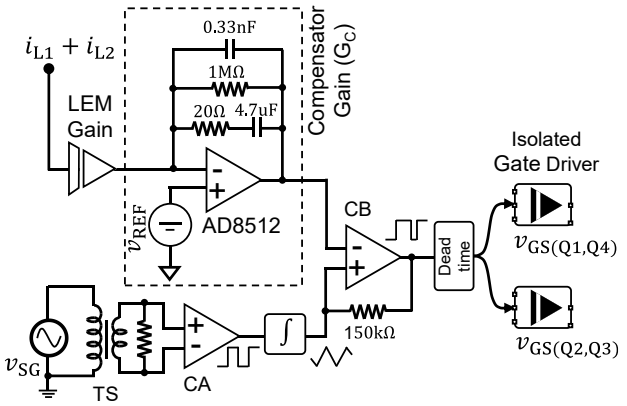

Fig. 8. Controller design and duty generation for a single cell of Class-PN.

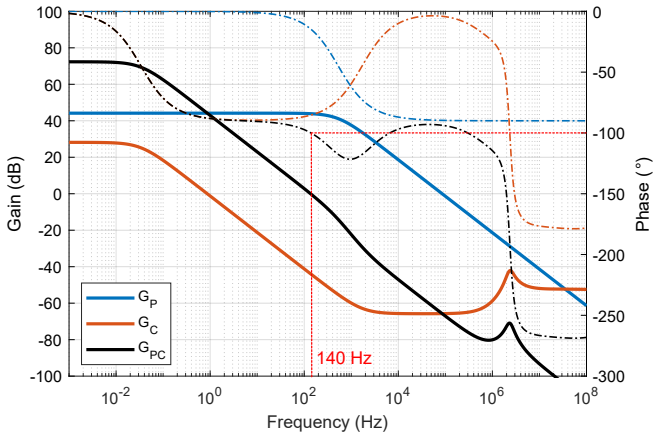

Fig. 9. Gain and phase for current-mode control of Class-PN.

cell of Class-PN. The output from LEM sensor is fed into a Type-II compensation network based on the very low noise, precision operation amplifier AD8512 from Analog Devices. A high resistance of 1 MΩ is placed to restrict the DC gain of the compensation network. A pole is placed at 10 kHz by the RC network of 20 Ω and 4.7 μH. And finally a high frequency noise filter capacitor of 0.33 nF is added. The compensation network is inspired from [36]. The output from compensation network is compared with a triangular waveform of frequency 6.78 MHz. The triangular waveform is generated from a sinusoidal signal of 6.78 MHz coming from an external signal generator (v_{SG}) as shown in Fig. 8. The signal generator supplies to the primary of a low power signal isolation transformer (TS). Current output from secondary of the signal isolation transformer is converted to voltage output through a tank resistor which is fed into the comparator (CA) to generate 50% duty cycle square wave of 6.78 MHz. The coupling capacitance between primary and secondary of signal isolation transformer is kept very low at 2 pF. This is important because the same signal generator v_{SG} is fed into all the cells in multi-cell configuration of Class-PN. Thus keeping the coupling capacitance to a minimum reduces conducted noise from propagating between the cells. The duty cycle adjusted PWM output from comparator (CB) is then fed into a dead time generation circuit that creates two complementary signals along with the specified dead time that is then provided to the isolated type gate drivers of GaN devices. The dead time generation circuit is based on quad 2-input NAND schmitt trigger. The dead time generation circuit works independently of the compensation network. This architecture is designed to eliminate the impact of propagation delay of the current sensor, controller and other ICs in the network. Details about the different ICs used in the controller and duty generation circuit is provided in Table III.

The compensator gain (G_C) along with the plant (G_P) and overall loop gain (G_{PC}) is plotted in Fig. 9. Based on G_{PC} the loop bandwidth is approximately 140 Hz. This gives a sufficient phase margin (ϕ_m) of 80°. The bandwidth of controller is designed to be low for two reasons.

1) As the load in industrial plant heats up, the load varies very slowly over several minutes thus a high bandwidth controller is not required.
2) Because each Class-PN cell in multi-cell configuration have their own independent controller, thus a fast response might lead to timing mismatch between the P-state and N-state.

V. Multi-Cell Operation of Class-PN

Section IV has explained in detail the design and development of a single Class-PN. This section will focus on extending the operation to multi-cell configuration based on the proposed series connection in Fig. 4(c). Fig. 10(a) shows multi-cell configuration of Class-PN. Three Class-PN cells are shown, where Cell 1 is closest to the input DC voltage (V_{DC}). The subsequent cells, Cell 2, and Cell 3 are connected to previous cells capacitor $C_{x\text{-}1}$, where x denotes cell position. The coupled inductors of the cells are connected directly to V_{DC}. As shown in section IV, the current of each cell's coupled inductors will be used to maintain its own capacitor voltage. For simplicity, only the coupled inductor current flow path for cell 2 is indicated here. Each of the cells in Fig. 10(a) have their own controller as presented in Section IV.B. The signal generator v_{SG} is provided to all three cells thus synchronising the P- and N-state.

Finally in Fig. 10(b) the output voltage seen by the load Z_{RF} is shown. During the N-state (d'T) the output voltage (v_{PN}) is the summation of voltages across capacitors C_1, C_2, and C_3. The current flow path during this time is highlighted in blue in Fig. 10(a). Similarly in the P-state (dT) the voltage across load will be the summation of voltages across DC, C_1, and C_2. The voltage transition is shown to occur during the dead time (T_d) as Class-PN is a voltage source type converter and achieves ZVS by inductive load current as discussed in section III.

VI. Operation and Experimental Results

For testing the multi-cell configuration of three Class-PN cells a high power load is designed using high power thick film type resistors of 470 Ω ±5%, 800 W [37]. Fig. 11(a) shows five of such thick film resistors attached to a copper

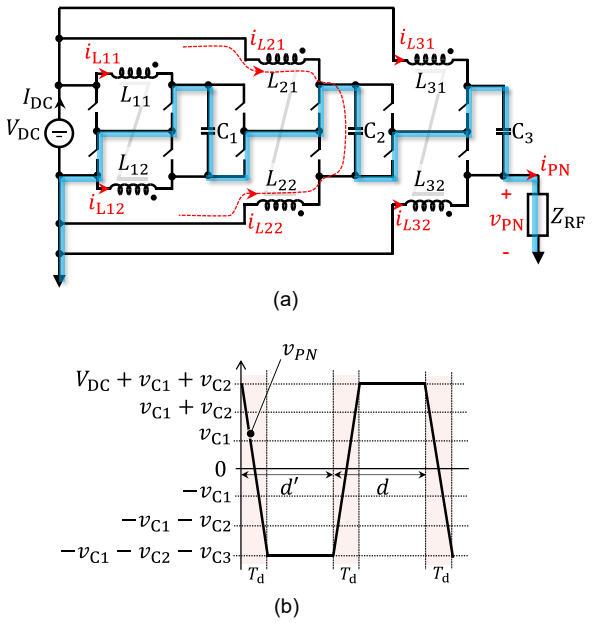

Fig. 10. (a) Parallel multi-cell configuration of three Class-PN cells, and (b) voltage seen by load Z_{RF}.

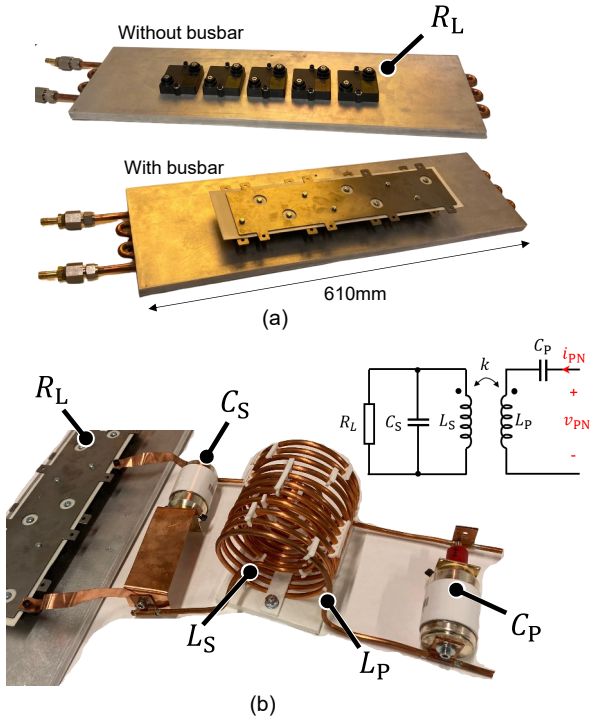

Fig. 11. (a) Thick film resistor based 4kW load (R_L) shown with and without busbar, (b) series-parallel resonant load network (Z_{RF}).

TABLE III
SYSTEM PARAMETER SUMMARY

Parameter	Value
Class-PN converter	
GaN devices	GS66506T (650 V, 22.5 A)
Gate driver	Si8271AB-IS (isolated type)
Thermal interface	Gap Pad® 5000S35 (5 W/mK)
Coontroller design and duty generation	
Comparator (CA, CB)	TLV3502 (high-speed comparator)
Compensator opamp	AD8512 (precision opamp)
Dead time circuit	74VHC132 (2-input NAND schmitt)
Current sensor	LEM HASS 50-S
Series-parallel resonant load	
Compensating capacitors (C_P, C_S)	CVUN-250AC/15-BAJA-2
Resistive load (R_L)	LPS 800 (470 Ω ±5%, 800 W)

tube based water cooled heatsink. A busbar is used to connect all five resistors in parallel that gives an equivalent resistance value of 93.5 Ω at 4 kW (R_L). The busbar is designed to add minimum parasitic capacitance and inductance. Fig. 11(b) shows the overall load network (Z_{RF}) along with R_L. It is a series-parallel resonant load where primary and secondary side compensation capacitors (C_P, C_S) are adjusted to be 114 pF, and 224 pF respectively. The series-parallel resonant load and Class-PN converter parameters are summarized in Table III.

An air-core transformer is developed for the series-parallel resonant load as shown in Fig. 11(b). The primary coil of the transformer has higher number of turns than secondary coil which sits within the primary in a helical structure. The designed transformer is tested for its primary and secondary coil inductance as well as series resistance (solid lines) using impedance analyzer Keysight E4990A and is presented in Fig. 12. The figure also contains COMSOL based multiphysics simulation (dotted lines) using the magnetic and electric fields physics toolbox. The simulation results agree closely with the measurement for both series resistance and self inductance of the primary coil. For example the COMSOL simulation predicted 170 mΩ primary coil series resistance at 7 MHz which matches precisely with the measured results. However the secondary coil results has a larger deviation that can be accounted to measurement errors due to smaller size of secondary coil. The air-core based design will eliminate core losses in the transformer and will account for very low conduction losses due low series resistance of approximately 200 mΩ in both primary and secondary coils. Fig. 13 shows the current density distribution of the air-core transformer at 7 MHz. The development of the load network is presented in detail in [20] where it is shown that the entire series-parallel load network is 98.3% efficient.

The load is designed to emulate the structure of an industrial dielectric heating plant. However it can be extended to also emulate induction heating application with necessary changes. The designed load remains constant throughout the operation. This is different from an actual industrial induction or dielectric load which will show dynamic behavior during the heating cycle and its value varies with the temperature. There are many methods to compensate a varying load such as dynamic tuning of a variable capacitor or an inductor in the load. The capacitive tuning method is shown in Fig. 2

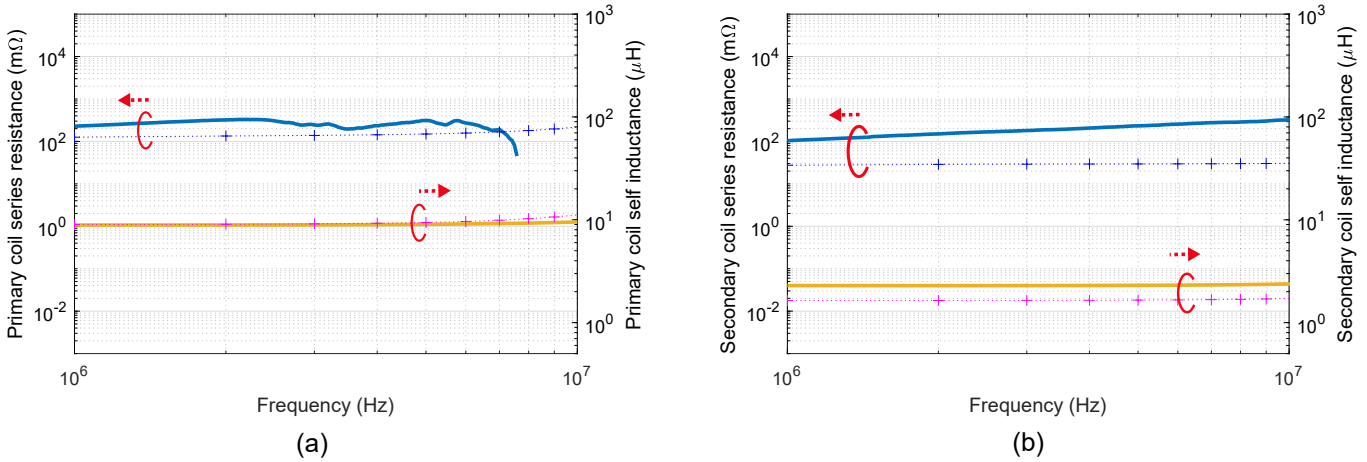

Fig. 12. Impedance analyzer (Keysight E4990A) measurement (solid) and COMSOL simulation (dotted) on air-core transformers (a) primary coil, and (b) secondary coil.

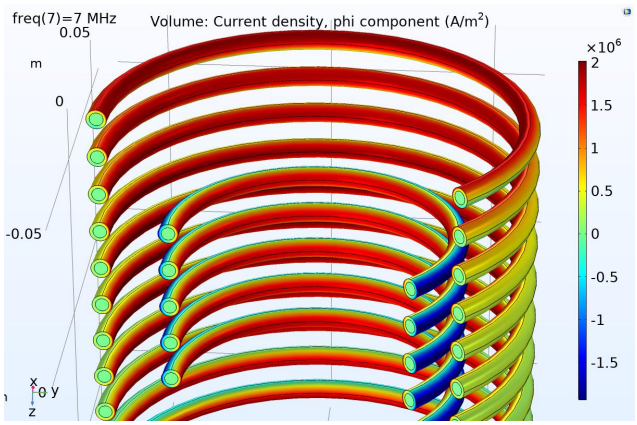

Fig. 13. COMSOL simulation of current density distribution in the primary and secondary coil at 7 MHz.

[5]. Variable inductor method for compensating variable load is presented in [6]. Third method to compensate for dynamic load is varying the switching frequency of the RF generator itself as presented in [38]. For this paper however the focus is on validating the multi-cell operation of Class-PN therefore the developed load shown in Fig. 11 is static in nature. Three Class-PN cells are connected in multi-cell configuration as discussed in section V and operated. Fig. 14 shows picture of the hardware setup of three cells, connected to the load network along with measurement voltage and current probes. Cell 1, 2, and 3 are connected to the V_{DC} via a busbar. The load network is connected to Cell 3 where the Class-PN RF generator output voltage v_{PN} and current i_{PN} are measured. A high voltage passive probe PPE6kV (400 MHz bandwidth) is used to measure v_{PN}. PPE6kV has a maximum DC+peak AC voltage rating of 6 kV until 10 MHz after which the voltage capability rolls off [39]. The Class-PN RF generator output current i_{PN} as well as input current i_{DC} are measured by clamp type hall effect probes CP030. These clamp probes has DC current capability of 30 A rms which rolls off beyond 1 kHz [40]. The current capability of CP030 is extremely limited at the operation frequency of 6.78 MHz therefore for further tests, higher rating current probes will be required. A high voltage differential probe (HVD3605A) is used to measure the load resistor (R_{L}) voltage. HVD3605A (100 MHz bandwidth) has a voltage measuring capability of 6 kV rms voltage until 200 kHz after which it rolls off to approximately 400 V rms at 7 MHz [41]. Similar to the current probe, the differential probe HVD3605A has also been a limiting factor for further tests. And therefore for future work, better probes will be acquired. All the probes and oscilloscope are from Teledyn Lecroy which provides good compatibility between the equipment.

Fig. 15(a), and (b) show experimental waveforms at V_{DC} of 185 V. Fig. 15(a) shows the RF generator output voltage v_{PN} that has peak-peak voltage of 1.1 kV. The load resistor voltage (v_{RL}) has a peak-peak value of 800 V which gives an output power of 856 W at 93.5 Ω. In Fig. 15(b), the current waveforms are shown, i_{PN} is the Class-PN output current whereas i_{DC} is the DC input current to the RF generator. Average value of i_{DC} is 5.8 A which gives an input power of 1.1 kW at 185 V V_{DC}. This includes the gate drive power as well. Thus the overall RF generator and load efficiency is approximately 80%.

VII. Discussion and Conclusion

Industrial induction and dielectric heating industry relies on vacuum tube triode for high voltage and high frequency output RF generator. Modern semiconductor technology, especially WBG devices such as SiC and GaN devices have achieved the high frequency output as required for industrial heating, however the high voltage and output power is still insufficient to replace triodes. To achieve this, in this paper a series connection method is proposed to scale-up the output voltage from semiconductor based RF generator. The proposed method is different from power combiner method as used in VHF and UHF applications. As the proposed method does not add additional components in the system and can be implemented as a turn-key solution in existing industrial heating plants.

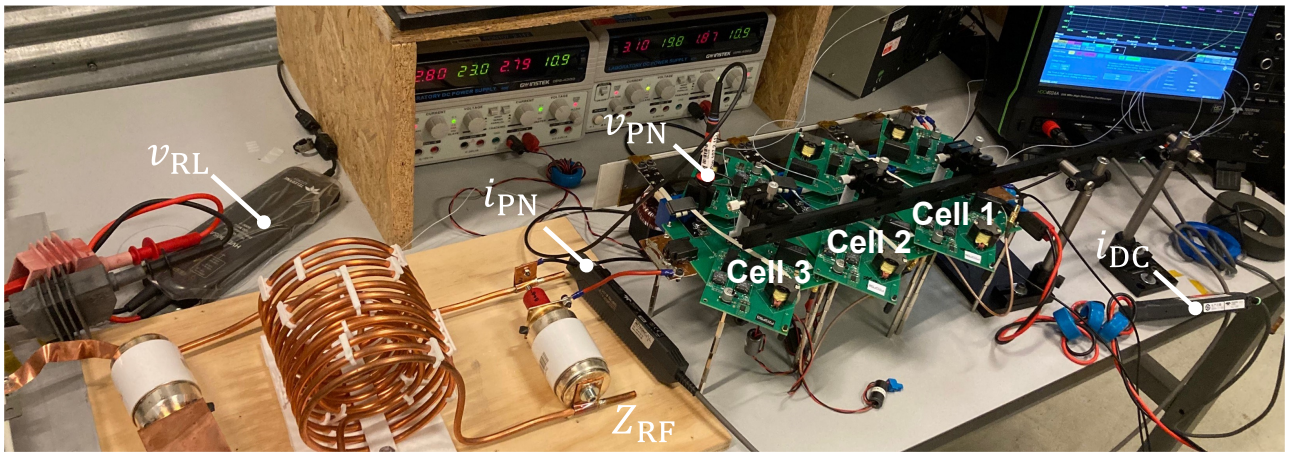

Fig. 14. Three Class-PN in multi-cell configuration connected to Z_{RF}, along with measurement probes.

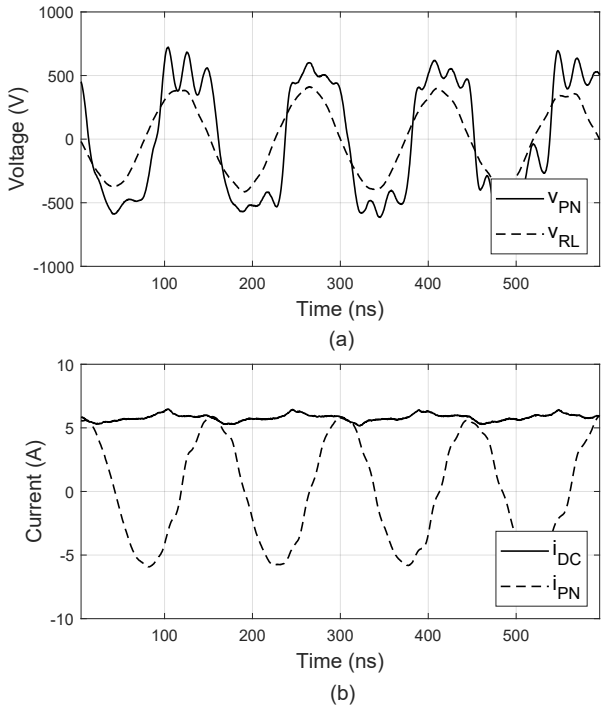

Fig. 15. Experimental results when operating three Class-PN in series connected multi-cell configuration (a) RF generator output voltage and load resistor voltage, and (b) RF generator input and output current.

Another consideration while selecting semiconductor device for the individual RF converter which has not been addressed in this paper is input junction capacitance (C_{ISS}). Selecting high current rated semiconductor devices will lead to high dissipation energy losses in output capacitance (C_{OSS}) as discussed in section III. Furthermore the high C_{ISS} value of high current rated devices will be a limiting factor in switching frequency capability. The gate loop RC time constant (τ) has to be less than $1/4^{th}$ the available turn-on time for a standard totem-pole gate driver to charge the gate to its nominal voltage. The gate loop time constant (τ) for the design in this work is 8.4 ns which leads to a value of 33.5 ns (4τ). Thus the GaN HEMT have been able to switch properly at 6.78 MHz with an available turn-on time of 60 ns in each half-cycle and 14 ns of dead time. However if we want to increase the switching frequency to 13.56 MHz, modifications to the gate loop is required either in the form of reduced gate resistance or smaller current rating GaN device.

Class-PN is used as the high frequency power amplifier due to its high power handling capability. A current-mode control is designed to maintain the capacitor voltage and ensure balanced operation in each individual RF converter without the need of inter-communication between the cells or with a central controller. The results achieved with three Class-PN cells validates the methodology proposed and achieves 1.1 kV peak-peak output voltage using 650 V GaN HEMT devices. It is to be pointed that the efficiency of 80% achieved in this paper is lower than other WBG device based works presented in state-of-art discussion in section II. This is due to the fact that results presented in this paper has been achieved at a low DC link voltage of 185 V. In a previous work a single Class-PN converter has been shown to achieve an efficiency of 90% [20]. Therefore by further increasing the DC link voltage and the number of cells, the proposed methodology of series connecting Class-PN can be considered as a candidate for GaN based RF generator suitable for the industrial heating industry.

REFERENCES

[1] A. Hasanbeigi, L. A. Kirshbaum, B. Collison, and D. Gardiner, "Electrifying U.S. Industry: A Technology- and Process-Based Approach to Decarbonization," *Renewable Thermal Collaborative*, 2021.

[2] U. S. DOE, "Improving Process Heating System Performance - A Sourcebook for Industry," *U.S. Department of Energy, Energy Efficiency and Renewable Energy*, 2015.

[3] E. Dede, J. Jordan, and V. Esteve, "State-of-the art and future trends in transistorised inverters for induction heating applications," in *Proceedings of the Fifth IEEE International Caracas Conference on Devices, Circuits and Systems, 2004.*, vol. 1, 2004, pp. 204–211.

[4] K. Dadzis, R. Menzel, M. Ziem, T. Turschner, H. Riemann, and N. V. Abrosimov, "High-frequency Heat Induction Modeling for a Novel Silicon Crystal Growth Method," in *Proceedings of the VIII International Scientific Colloquim "Modelling for Materials Processing"*, 2017, pp. 31–36.

[5] H. F. Dittrich, "Tubes for R.F. Heating," *Application Book, Electronic Components and Materials Division Philips*, 1971.

[6] T. Koral, "Radio Frequency Heating and Post-Baking - A maturing Technology that can still offer significant benefits," *Biscuit World*, vol. 7, no. 4, 2004.

[7] G. W. Scott, "Induction and Dielectric Heating," *Transactions of the American Institute of Electrical Engineers*, vol. 67, no. 2, pp. 885–892, 1948.

[8] T. L. Wilson, "Radio-Frequency Dielectric Heating in Industry," *Electric Power Research Institute, California, USA*, 3 1987.

[9] I. Corporation, "3kW and 5kW half-bridge Class-D RF generators at 13.56MHz and 89% efficiency and limited frequency agility," 2002. [Online]. Available: https://notes-application.abcelectronique.com/092/92-59735.pdf

[10] ——, "PRF-1150 1 KW 13.56 MHz Class E RF Generator Evaluation Module," 2019. [Online]. Available: https://www.mouser.com/datasheet/2/205/apprf_1150_ClassE_RF_Generator_Module_App_Note-1-1308042.pdf

[11] S. Aldhaher, D. C. Yates, and P. D. Mitcheson, "Modeling and Analysis of Class EF and Class E/F Inverters With Series-Tuned Resonant Networks," *IEEE Transactions on Power Electronics*, vol. 31, no. 5, pp. 3415–3430, 2016.

[12] J. Choi, D. Tsukiyama, Y. Tsuruda, and J. Rivas, "13.56 MHz 1.3 kW resonant converter with GaN FET for wireless power transfer," in *2015 IEEE Wireless Power Transfer Conference (WPTC)*, 2015, pp. 1–4.

[13] S. Guo, L. Zhang, Y. Lei, X. Li, F. Xue, W. Yu, and A. Q. Huang, "3.38 Mhz operation of 1.2kV SiC MOSFET with integrated ultra-fast gate drive," in *2015 IEEE 3rd Workshop on Wide Bandgap Power Devices and Applications (WiPDA)*, 2015, pp. 390–395.

[14] J. Choi, D. Tsukiyama, and J. Rivas, "Evaluation of a 900 V SiC MOSFET in a 13.56 MHz 2 kW resonant inverter for wireless power transfer," in *2016 IEEE 17th Workshop on Control and Modeling for Power Electronics (COMPEL)*, 2016, pp. 1–6.

[15] A. B. Jorgensen, U. R. Nair, S. Munk-Nielsena, and C. Uhrenfeldt, "A SiC MOSFET Power Module With Integrated Gate Drive for 2.5 MHz Class E Resonant Converters," in *CIPS 2018; 10th International Conference on Integrated Power Electronics Systems*, 2018, pp. 1–6.

[16] J. M. Arteaga, S. Aldhaher, G. Kkelis, D. C. Yates, and P. D. Mitcheson, "Multi-MHz IPT Systems for Variable Coupling," *IEEE Transactions on Power Electronics*, vol. 33, no. 9, pp. 7744–7758, 2018.

[17] L. Gu and J. Rivas-Davila, "1.7 kW 6.78 MHz Wireless Power Transfer with Air-Core Coils at 95.7% DC-DC Efficiency," in *2021 IEEE Wireless Power Transfer Conference (WPTC)*, 2021, pp. 1–4.

[18] T. S. Aunsborg, S. B. Duun, S. Munk-Nielsen, and C. Uhrenfeldt, "Development of a Current Source Resonant Inverter for High Current MHz Induction Heating," *IET power electronics*, vol. 15, no. 1, p. 1–10, 2022.

[19] T. S. Aunsborg, B. Bidoggia, S. B. Duun, B. F. Kjærsgaard, J. D. Meinert, A. B. Jørgensen, and S. Munk-Nielsen, "Demonstration of a Class E push-pull resonant inverter for MHz induction heating," in *2023 IEEE Applied Power Electronics Conference and Exposition (APEC)*, 2023, pp. 705–709.

[20] F. Ahmad, A. B. Jørgensen, and S. Munk-Nielsen, "Modeling and Operation of Series-Parallel Resonant Load in Industrial RF Dielectric Heating Application," *IEEE Transactions on Industry Applications*, vol. 59, no. 4, pp. 4418–4428, 2023.

[21] A. Jain, P. R. Hannurkar, D. K. Sharma, A. K. Gupta, A. K. Tiwari, M. Lad, R. Kumar, P. D. Gupta, and S. K. Pathak, "Design and characterization of 50 kW solid-state RF amplifier," *International Journal of Microwave and Wireless Technologies*, vol. 4, no. 6, p. 595–603, 2012.

[22] A. Al Bastami, H. Zhang, A. Jurkov, A. Radomski, and D. Perreault, "Comparison of Radio-Frequency Power Architectures for Plasma Generation," in *2020 IEEE 21st Workshop on Control and Modeling for Power Electronics (COMPEL)*, 2020, pp. 1–8.

[23] S. Jeon and D. Rutledge, "A 2.7-kW, 29-MHz Class-E/F$_{odd}$ Amplifier with a Distributed Active Transformer," in *IEEE MTT-S International Microwave Symposium Digest, 2005.*, 2005, pp. 1927–1930.

[24] F. Ahmad, A. B. Jørgensen, and S. Munk-Nielsen, "Multi-cell Operation of Class-PN at 6.78 MHz using GaN Devices for Industrial Dielectric Heating," in *2023 11th International Conference on Power Electronics and ECCE Asia (ICPE 2023 - ECCE Asia)*, 2023, pp. 120–125.

[25] N. Perera, M. S. Nikoo, A. Jafari, L. Nela, and E. Matioli, "C_{oss} Loss Tangent of Field-Effect Transistors: Generalizing High-Frequency Soft-Switching Losses," *IEEE Transactions on Power Electronics*, vol. 35, no. 12, pp. 12 585–12 589, 2020.

[26] M. Guacci, M. Heller, D. Neumayr, D. Bortis, J. W. Kolar, G. Deboy, C. Ostermaier, and O. Häberlen, "On the Origin of the C_{oss} -Losses in Soft-Switching GaN-on-Si Power HEMTs," *IEEE Journal of Emerging and Selected Topics in Power Electronics*, vol. 7, no. 2, pp. 679–694, 2019.

[27] O. Knecht, R. Bosshard, and J. W. Kolar, "High-Efficiency Transcutaneous Energy Transfer for Implantable Mechanical Heart Support Systems," *IEEE Transactions on Power Electronics*, vol. 30, no. 11, pp. 6221–6236, 2015.

[28] F. Ahmad, A. B. Jørgensen, and S. Munk-Nielsen, "Four-switch Class-PN Power Amplifier for High Power Handling Capability in Wireless Power Transfer," in *2022 International Power Electronics Conference (IPEC-Himeji 2022- ECCE Asia)*, 2022, pp. 968–972.

[29] GaN Systems, "Top-side cooled 650V E-mode GaN transistor," 2022. [Online]. Available: https://gansystems.com/wp-content/uploads/2020/04/GS66506T-DS-Rev-200402.pdf

[30] ——, "GN002 Application Note - Thermal Design GaNPX®Packaged Devices," accessed: January, 2024. [Online]. Available: https://gansystems.com/wp-content/uploads/2018/10/GN002_Thermal-Design-Guide-for-Top-Side-Cooled-GaNpx-T-Devices_Rev-181030.pdf

[31] The Bergquist Company, "Gap Pad 5000S35," accessed: January, 2024. [Online]. Available: https://www.farnell.com/datasheets/1323705.pdf

[32] F. Ahmad, T. S. Aunsborg, S. M. Beczkowski, S. Munk-Nielsen, and A. B. Jorgensen, "Thermal Performance of an Integrated Heat Spreader for GaN HEMT devices," in *CIPS 2022; 12th International Conference on Integrated Power Electronics Systems*, 2022, pp. 1–6.

[33] A. B. Jørgensen, T.-H. Cheng, D. Hopkins, S. Beczkowski, C. Uhrenfeldt, and S. Munk-Nielsen, "Thermal Characteristics and Simulation of an Integrated GaN eHEMT Power Module," in *2019 21st European Conference on Power Electronics and Applications (EPE '19 ECCE Europe)*, 2019, pp. P.1–P.7.

[34] J. S. Glaser and J. M. Rivas, "A 500 W push-pull dc-dc power converter with a 30 MHz switching frequency," in *2010 Twenty-Fifth Annual IEEE Applied Power Electronics Conference and Exposition (APEC)*, 2010, pp. 654–661.

[35] Micrometals - Powder Core Solutions, "T200-2," 2022, [Online; accessed Jan 2023]. [Online]. Available: https://datasheets.micrometals.com/T200-2-DataSheet.pdf

[36] H. J. Zhang, "Modeling and Loop Compensation Design of Switching Mode Power Supplies," *Linear Technology - Application Note 149*, January 2015.

[37] Vishay Sfernice, "LPS 800," https://www.vishay.com/docs/50054/lps800.pdf, 2021, [Online; accessed Nov 2022].

[38] S. Dieckerhoff, M. Ruan, and R. De Doncker, "Design of an IGBT-based LCL-resonant inverter for high-frequency induction heating," in *Conference Record of the 1999 IEEE Industry Applications Conference. Thirty-Forth IAS Annual Meeting (Cat. No.99CH36370)*, vol. 3, 1999, pp. 2039–2045 vol.3.

[39] Teledyne Lecroy, "High Voltage PPE 6 kV," 2024, [Online; accessed January 2024]. [Online]. Available: https://www.mouser.dk/datasheet/2/227/ppe_6kv_user_manual-179980.pdf

[40] ——, "Current Probes," 2022, [Online; accessed June 2022]. [Online]. Available: https://cdn.teledynelecroy.com/files/pdf/current-probes-datasheet.pdf

[41] ——, "High Voltage Differential Probes," 2022, [Online; accessed June 2022]. [Online]. Available: https://cdn.teledynelecroy.com/files/pdf/hvd3000a-probes-datasheet.pdf

Faheem Ahmad Faheem Ahmad received the B.Sc. degree in Electrical Engineering from Delhi Technological University, Delhi India in 2014. He later recieved the M.Sc. degree in Energy Engineering with a specialization in power electronics and drives in 2020 and Ph.D. in power electronics in 2023 from Aalborg University, Aalborg, Denmark.

He is currently working as a Postdoctoral researcher at AAU Energy, Aalborg University. He previously worked with Toshiba Semiconductors as Systems Engineer on residential solar inverters between 2015-2018. His research interests include high frequency converter topology, resonant converters, and wide bandgap power semiconductors.

Thore Stig Aunsborg Thore Stig Aunsborg (Student Member, IEEE) received the M.Sc. degree in nanophysics and material science in 2016 from Aalborg University, Aalborg, Denmark, and the Ph.D. degree in power electronic converter design with AAU Energy in 2023. His research interests include high frequency resonant converters, wideband gap devices, medium voltage power converters, and power module packaging.

Asger Bjørn Jørgensen Asger Bjørn Jørgensen received the M.Sc. degree in energy engineering with a specialization in power electronics and the Ph.D. degree from Aalborg University, Aalborg, Denmark, in 2016 and 2019, respectively.

He is currently a Assistant Professor at AAU Energy, Aalborg University. His research interests include power module packaging, wide bandgap power semiconductors, and multiphysics finite element analysis.

Stig Munk-Nielsen Stig Munk-Nielsen (Member, IEEE) received the M.Sc. and Ph.D. degrees from Aalborg University, Aalborg, Denmark, in 1991 and 1997, respectively.

He is currently a Professor at AAU Energy, Aalborg University. His research interests include LV and MV Si, SiC, and GaN converters, packaging of power electronic devices, electrical monitoring apparatus for IGBTs, failure modes, and device test systems. In the last ten years, he has been involved in or has managed ten research projects and has authored or coauthored 242 international power electronic papers.